

KEK-TH-808  
hep-ph/0203110

# Detailed calculation of lepton flavor violating muon-electron conversion rate for various nuclei

Ryuichiro Kitano,<sup>ab,\*</sup> Masafumi Koike,<sup>a,†</sup> and Yasuhiro Okada<sup>ab,‡</sup>

<sup>a</sup>*Theory Group, KEK, Oho 1-1, Tsukuba, Ibaraki 305-0801, Japan*

<sup>b</sup>*Department of Particle and Nuclear Physics, The Graduate University for Advanced Studies, Oho 1-1, Tsukuba, Ibaraki 305-0801, Japan*

February 8, 2020

## Abstract

The coherent  $\mu$ - $e$  conversion rates in various nuclei are calculated for general lepton flavor violating interactions. We solve the Dirac equations numerically for the initial state muon and the final state electron in the Coulomb force, and perform the overlap integrals between the wave functions and the nucleon densities. The results indicate that the conversion branching ratio increases for a light nucleus up to the atomic number  $Z \sim 30$ , is largest for  $Z = 30 - 60$ , and becomes smaller for a heavy nucleus with  $Z \gtrsim 60$ . We also discuss the uncertainty from the input proton and neutron densities. The atomic number dependence of the conversion ratio calculated here is useful to distinguish theoretical models with lepton flavor violation.

---

\*email: ryuichiro.kitano@kek.jp

†email: mkoike@post.kek.jp

‡email: yasuhiro.okada@kek.jp

# 1 Introduction

The observation of lepton flavor violation (LFV) is one of the most interesting signals beyond the Standard Model (SM). The charged-lepton LFV processes such as the  $\mu \rightarrow e\gamma$  decay and the  $\mu$ - $e$  conversion in muonic atoms can occur in many promising candidates beyond the SM, although the simple seesaw neutrino model does not induce experimentally observable rate for the  $\mu \rightarrow e\gamma$  process. For example, sleptons in the supersymmetric (SUSY) extension of the SM and bulk neutrinos in the higher dimensional models generate LFV processes through one-loop diagrams [1, 2]. In the R-parity violating SUSY models, additional LFV interactions exist at the tree level [3]. The branching ratios of the LFV processes have been calculated in many models in the literature, especially for supersymmetric grand unified theories (SUSY-GUTs) [4, 5] and a SUSY model with right-handed neutrinos [6]. It was shown that  $\mu \rightarrow e\gamma$  and  $\mu$ - $e$  conversion branching ratios can be close to the experimental bounds in these models.

There are on-going and planned experiments for the  $\mu \rightarrow e\gamma$  and  $\mu$ - $e$  conversion searches. For the  $\mu \rightarrow e\gamma$  branching ratio, the present upper bound is  $1.2 \times 10^{-11}$  from the MEGA collaboration [7]. A new experiment is under construction at PSI aiming for a sensitivity of  $10^{-14}$  [8]. For the  $\mu$ - $e$  conversion, an upper bound for the conversion branching ratio is  $6.1 \times 10^{-13}$  [9] reported by the SINDRUM II experiment at PSI. Now SINDRUM II is running with gold (Au) targets. The MECO experiment at BNL [10] are planned in order to search for  $\mu\text{Al} \rightarrow e\text{Al}$  with a sensitivity below  $10^{-16}$ . In future, further improvements by one or two orders of magnitude are considered for both  $\mu \rightarrow e\gamma$  and  $\mu$ - $e$  conversion processes in the PRISM project [11] at the new 50 GeV proton synchrotron constructed as a part of the JAERI/KEK joint project.

In order to compare the sensitivity to the LFV interaction in various nuclei, precise calculation of the  $\mu$ - $e$  conversion rate is necessary. There have been several calculations of the conversion rate. Weinberg and Feinberg calculated in the case that the conversion occurs through the photonic interactions ( $\mu$ - $e$ - $\gamma$  vertex) [12]. In the calculation, they used several approximations in which the muon wave function was taken to be constant in a nucleus and the outgoing electron was treated as a plane wave. The plane wave treatment of the electron is a good approximation only for light nuclei because the effect of Coulomb distortion on the electron wave function is large for heavy targets. The non-

photonic interaction case was calculated by Marciano and Sanda [13]. Shanker improved the calculation by solving the Dirac equations for the muon and electron wave functions in the electric potential of a nucleus [14]. The calculation was carried out for all the interactions including the photonic and four-fermion operators in the effective Lagrangian, but the treatment of the photonic dipole operator was incomplete because he used an approximation that off-shell photon exchange was replaced by the four-fermion interaction. Recently, Czarnecki *et al.* presented calculation in which the off-shell photon is properly treated as an electric field in a nucleus and listed the values of the conversion rate for aluminum (Al), titanium (Ti), and lead (Pb) targets [15]. The transition rate to the ground state of a nucleus as well as excited states are calculated in Refs.[16, 17].

In this paper, we evaluated the  $\mu$ - $e$  conversion rates for nuclei of a wide range of atomic numbers by the method of Czarnecki *et al.* We took into account all the operators for the  $\mu$ - $e$  transition. For any types of operators, the results of our calculation indicate a tendency that the conversion branching ratio is larger for the nuclei with moderate atomic numbers than that for light or heavy nuclei. Although the tendency is the same, there are significant differences in  $Z$  dependences of the conversion rate for various LFV couplings. The experiments in various nuclei are therefore useful for model discrimination because each theoretical model predicts different  $Z$  dependences. The conversion rate depends on the input proton and neutron densities for each nucleus. Although the proton density is well measured by the electron scattering, there is large uncertainty in determination of neutron densities. We estimate the uncertainty due to these input parameters and show that the conversion rate for heavy nuclei changes by 20% – 30% due to the ambiguity of neutron density distribution.

This paper is organized as follows. In section 2, we present a formula of the conversion rate with the most general effective Lagrangian for LFV. The results of our calculation and the estimation of the uncertainty are shown in section 3. In section 4, we summarize this paper. The model parameters of the nucleon density functions in nuclei and the muon capture rate in nuclei are listed in Appendices A and B, respectively.

## 2 Formula of $\mu$ - $e$ conversion rate

In this section, we present a method of the conversion rate calculation. We solve the Dirac equations for the muon and electron in the initial and final states, respectively, and obtain transition amplitudes by integrating the overlap of the both wave functions.

We start with the most general LFV interaction Lagrangian which contributes to the  $\mu$ - $e$  transition in nuclei [1]:

$$\begin{aligned} \mathcal{L}_{\text{int}} = & -\frac{4G_F}{\sqrt{2}} (m_\mu A_R \bar{\mu} \sigma^{\mu\nu} P_L e F_{\mu\nu} + m_\mu A_L \bar{\mu} \sigma^{\mu\nu} P_R e F_{\mu\nu} + \text{h.c.}) \\ & -\frac{G_F}{\sqrt{2}} \sum_{q=u,d,s} \left[ (g_{LS(q)} \bar{e} P_R \mu + g_{RS(q)} \bar{e} P_L \mu) \bar{q} q \right. \\ & \quad + (g_{LP(q)} \bar{e} P_R \mu + g_{RP(q)} \bar{e} P_L \mu) \bar{q} \gamma_5 q \\ & \quad + (g_{LV(q)} \bar{e} \gamma^\mu P_L \mu + g_{RV(q)} \bar{e} \gamma^\mu P_R \mu) \bar{q} \gamma_\mu q \\ & \quad + (g_{LA(q)} \bar{e} \gamma^\mu P_L \mu + g_{RA(q)} \bar{e} \gamma^\mu P_R \mu) \bar{q} \gamma_\mu \gamma_5 q \\ & \quad \left. + \frac{1}{2} (g_{LT(q)} \bar{e} \sigma^{\mu\nu} P_R \mu + g_{RT(q)} \bar{e} \sigma^{\mu\nu} P_L \mu) \bar{q} \sigma_{\mu\nu} q + \text{h.c.} \right], \quad (1) \end{aligned}$$

where  $G_F$  and  $m_\mu$  are the Fermi constant and the muon mass, respectively, and  $A_{L,R}$  and  $g$ 's are all dimensionless coupling constants for the corresponding operators. Our conventions are  $F_{\mu\nu} = \partial_\mu A_\nu - \partial_\nu A_\mu$ ,  $\sigma^{\mu\nu} = (i/2)[\gamma^\mu, \gamma^\nu]$ ,  $P_L = (1 - \gamma_5)/2$ ,  $P_R = (1 + \gamma_5)/2$ , and the covariant derivative is defined as  $D_\mu = \partial_\mu - iQeA_\mu$ , where  $Qe$  ( $e > 0$ ) is the electric charge ( $Q = -1$  for the electron and the muon). The size of each coupling constant depends on the interaction of the new physics in which the lepton flavor conservation is violated. There are two types of the amplitudes for photonic transition ( $\mu$ - $e$ - $\gamma$ ), namely the monopole and dipole  $\mu$ - $e$  transitions. In the above expression, the monopole transition is converted to the vector-vector interaction assuming that the momentum dependences of the form factors are negligible.

The initial state in the  $\mu$ - $e$  conversion process is the  $1s$  state of the muonic atom, and the final electron state is the eigenstate with an energy of  $m_\mu - \epsilon_b$ , where  $\epsilon_b$  is the binding energy of the  $1s$  muonic atom. Both wave functions in the initial and final states can be determined by solving the Dirac equations in the electric field of the nucleus. The Dirac

equation in the central force system is given by [18]

$$W\psi = \left[ -i\gamma_5\sigma_r \left( \frac{\partial}{\partial r} + \frac{1}{r} - \frac{\beta}{r}K \right) + V(r) + m_i\beta \right] \psi, \quad (2)$$

$$\gamma_5 = \begin{pmatrix} 0 & 1 \\ 1 & 0 \end{pmatrix}, \quad \beta = \begin{pmatrix} 1 & 0 \\ 0 & -1 \end{pmatrix}, \quad \sigma_r = \begin{pmatrix} \boldsymbol{\sigma} \cdot \mathbf{r} & 0 \\ 0 & \boldsymbol{\sigma} \cdot \mathbf{r} \end{pmatrix},$$

$$K = \begin{pmatrix} \boldsymbol{\sigma} \cdot \mathbf{l} + 1 & 0 \\ 0 & -(\boldsymbol{\sigma} \cdot \mathbf{l} + 1) \end{pmatrix}, \quad (3)$$

where  $W$  and  $V(r)$  are the energy and potential, respectively,  $m_i$  is the reduced mass of the electron or the muon,  $\boldsymbol{\sigma}$  are the Pauli matrices, and the orbital angular momentum  $\mathbf{l}$  is defined by  $-i\mathbf{r} \times \nabla$ . Since the operator  $K$  and the  $z$ -component of the total angular momentum  $j_z$  commute with the Hamiltonian, two eigenvalues of these operators,  $-\kappa$  and  $\mu$ , represent the quantum numbers of the wave functions describing this system. We denote the wave function as follows:

$$\psi = \psi_\kappa^\mu = \begin{pmatrix} g(r)\chi_\kappa^\mu(\theta, \phi) \\ if(r)\chi_{-\kappa}^\mu(\theta, \phi) \end{pmatrix}, \quad (4)$$

where  $\chi_\kappa^\mu$  is the normalized eigenfunction of  $(\boldsymbol{\sigma} \cdot \mathbf{l} + 1)$  and  $j_z$  such as

$$(\boldsymbol{\sigma} \cdot \mathbf{l} + 1)\chi_\kappa^\mu = -\kappa\chi_\kappa^\mu, \quad j_z\chi_\kappa^\mu = \mu\chi_\kappa^\mu, \quad \int_{-1}^1 d\cos\theta \int_0^{2\pi} d\phi \chi_\kappa^{\mu*}\chi_{\kappa'}^{\mu'} = \delta_{\mu\mu'}\delta_{\kappa\kappa'} . \quad (5)$$

The total angular momentum  $j$  is related to  $\kappa$  as  $\kappa = \pm(j + 1/2)$ . With the notation of  $u_1(r) = rg(r)$  and  $u_2(r) = rf(r)$ , the Dirac equation for the radial function is given by

$$\frac{d}{dr} \begin{pmatrix} u_1 \\ u_2 \end{pmatrix} = \begin{pmatrix} -\kappa/r & W - V + m_i \\ -(W - V - m_i) & \kappa/r \end{pmatrix} \begin{pmatrix} u_1 \\ u_2 \end{pmatrix} . \quad (6)$$

The initial muon state corresponds to the quantum numbers of  $\mu = \pm 1/2$  and  $\kappa = -1$  with a normalization of

$$\int d^3x \psi_{1s}^{(\mu)*}(\mathbf{x})\psi_{1s}^{(\mu)}(\mathbf{x}) = 1 . \quad (7)$$

The final electron state is one of the states in the continuum spectrum. Our normalization convention is taken as

$$\int d^3x \psi_{\kappa,W}^{\mu(e)*}(\mathbf{x})\psi_{\kappa',W'}^{\mu'(e)}(\mathbf{x}) = 2\pi\delta_{\mu\mu'}\delta_{\kappa\kappa'}\delta(W - W') . \quad (8)$$

The conversion rate  $\omega_{\text{conv}}$  in this normalization is simply written by the square of the  $\mu$ - $e$  conversion amplitude  $M$ , taking the spin average of the initial muon and summing over the final states of the electron. From the effective Lagrangian (1),  $M$  is obtained as follows:

$$\begin{aligned}
M = & \frac{4G_F}{\sqrt{2}} \int d^3x \left( m_\mu A_R^* \bar{\psi}_{\kappa, W}^{\mu(e)} \sigma^{\alpha\beta} P_R \psi_{1s}^{(\mu)} + m_\mu A_L^* \bar{\psi}_{\kappa, W}^{\mu(e)} \sigma^{\alpha\beta} P_L \psi_{1s}^{(\mu)} \right) \langle N' | F_{\alpha\beta} | N \rangle \\
& + \frac{G_F}{\sqrt{2}} \sum_{q=u, d, s} \int d^3x \left[ \left( g_{LS(q)} \bar{\psi}_{\kappa, W}^{\mu(e)} P_R \psi_{1s}^{(\mu)} + g_{RS(q)} \bar{\psi}_{\kappa, W}^{\mu(e)} P_L \psi_{1s}^{(\mu)} \right) \langle N' | \bar{q}q | N \rangle \right. \\
& \quad + \left( g_{LP(q)} \bar{\psi}_{\kappa, W}^{\mu(e)} P_R \psi_{1s}^{(\mu)} + g_{RP(q)} \bar{\psi}_{\kappa, W}^{\mu(e)} P_L \psi_{1s}^{(\mu)} \right) \langle N' | \bar{q}\gamma_5 q | N \rangle \\
& \quad + \left( g_{LV(q)} \bar{\psi}_{\kappa, W}^{\mu(e)} \gamma^\alpha P_L \psi_{1s}^{(\mu)} + g_{RV(q)} \bar{\psi}_{\kappa, W}^{\mu(e)} \gamma^\alpha P_R \psi_{1s}^{(\mu)} \right) \langle N' | \bar{q}\gamma_\alpha q | N \rangle \\
& \quad + \left( g_{LA(q)} \bar{\psi}_{\kappa, W}^{\mu(e)} \gamma^\alpha P_L \psi_{1s}^{(\mu)} + g_{RA(q)} \bar{\psi}_{\kappa, W}^{\mu(e)} \gamma^\alpha P_R \psi_{1s}^{(\mu)} \right) \langle N' | \bar{q}\gamma_\alpha \gamma_5 q | N \rangle \\
& \quad \left. + \frac{1}{2} \left( g_{LT(q)} \bar{\psi}_{\kappa, W}^{\mu(e)} \sigma^{\alpha\beta} P_R \psi_{1s}^{(\mu)} + g_{RT(q)} \bar{\psi}_{\kappa, W}^{\mu(e)} \sigma^{\alpha\beta} P_L \psi_{1s}^{(\mu)} \right) \langle N' | \bar{q}\sigma_{\alpha\beta} q | N \rangle \right], \tag{9}
\end{aligned}$$

where  $\langle N' |$  and  $| N \rangle$  are the final and initial states of the nucleus, respectively.

Hereafter, we concentrate on the coherent conversion processes in which the final state of the nucleus is the same as the initial one. The fraction of the coherent process is generally larger than the in coherent one approximately by a factor of the mass number of the target nuclei. In this case, the matrix elements of  $\langle N | \bar{q}\gamma_5 q | N \rangle$ ,  $\langle N | \bar{q}\gamma_\alpha \gamma_5 q | N \rangle$ , and  $\langle N | \bar{q}\sigma_{\alpha\beta} q | N \rangle$  vanish identically, and  $\langle N | \bar{q}q | N \rangle$  and  $\langle N | \bar{q}\gamma_\alpha q | N \rangle$  can be expressed by the proton and neutron densities ( $\rho^{(p)}$  and  $\rho^{(n)}$ ) in nuclei as follows:

$$\langle N | \bar{q}q | N \rangle = Z c_p^{(q)} \rho^{(p)} + (A - Z) c_n^{(q)} \rho^{(n)}, \tag{10}$$

$$\langle N | \bar{q}\gamma^0 q | N \rangle = \begin{cases} 2Z\rho^{(p)} + (A - Z)\rho^{(n)} & \text{for } q = u, \\ Z\rho^{(p)} + 2(A - Z)\rho^{(n)} & \text{for } q = d, \\ 0 & \text{for } q = s, \end{cases} \tag{11}$$

$$\langle N | \bar{q}\gamma^i q | N \rangle = 0 \quad (i = 1, 2, 3). \tag{12}$$

Here we define coefficients  $c_{p,n}^{(q)}$  for scalar operators. These are evaluated to be  $c_{p,n}^{(u)} = 5.1$ ,  $c_{p,n}^{(d)} = 4.3$ , and  $c_{p,n}^{(s)} = 2.5$  in Kosmas *et al.* [19]. We assume that the proton and neutron

densities are spherically symmetric and normalized as follows:

$$\int_0^\infty dr 4\pi r^2 \rho^{(p,n)}(r) = 1 . \quad (13)$$

The final formula of the conversion rate can be written as follows:

$$\begin{aligned} \omega_{\text{conv}} &= 2G_F^2 \left| A_R^* D + \tilde{g}_{LS}^{(p)} S^{(p)} + \tilde{g}_{LS}^{(n)} S^{(n)} + \tilde{g}_{LV}^{(p)} V^{(p)} + \tilde{g}_{LV}^{(n)} V^{(n)} \right|^2 \\ &+ 2G_F^2 \left| A_L^* D + \tilde{g}_{RS}^{(p)} S^{(p)} + \tilde{g}_{RS}^{(n)} S^{(n)} + \tilde{g}_{RV}^{(p)} V^{(p)} + \tilde{g}_{RV}^{(n)} V^{(n)} \right|^2 . \end{aligned} \quad (14)$$

The coupling constants  $\tilde{g}$ 's in Eq.(14) are defined as

$$\tilde{g}_{LS,RS}^{(p,n)} = \sum_q c_{p,n}^{(q)} g_{LS,RS(q)} , \quad (15)$$

$$\tilde{g}_{LV,RV}^{(p)} = 2g_{LV,RV(u)} + g_{LV,RV(d)} , \quad (16)$$

$$\tilde{g}_{LV,RV}^{(n)} = g_{LV,RV(u)} + 2g_{LV,R(d)} . \quad (17)$$

We also introduced the following overlap integrals:

$$D = \frac{4}{\sqrt{2}} m_\mu \int_0^\infty dr r^2 [-E(r)] (g_e^- f_\mu^- + f_e^- g_\mu^-) , \quad (18)$$

$$S^{(p)} = \frac{1}{2\sqrt{2}} \int_0^\infty dr r^2 Z \rho^{(p)} (g_e^- g_\mu^- - f_e^- f_\mu^-) , \quad (19)$$

$$S^{(n)} = \frac{1}{2\sqrt{2}} \int_0^\infty dr r^2 (A - Z) \rho^{(n)} (g_e^- g_\mu^- - f_e^- f_\mu^-) , \quad (20)$$

$$V^{(p)} = \frac{1}{2\sqrt{2}} \int_0^\infty dr r^2 Z \rho^{(p)} (g_e^- g_\mu^- + f_e^- f_\mu^-) , \quad (21)$$

$$V^{(n)} = \frac{1}{2\sqrt{2}} \int_0^\infty dr r^2 (A - Z) \rho^{(n)} (g_e^- g_\mu^- + f_e^- f_\mu^-) , \quad (22)$$

where the functions  $g_e^-$  etc. are defined in the  $1s$  muon wave function and  $\kappa = \pm 1$  electron wave functions as follows:

$$\psi_{1s}^{(\mu)}(r, \theta, \phi) = \begin{pmatrix} g_\mu^-(r) \chi_{-1}^{\pm 1/2}(\theta, \phi) \\ i f_\mu^-(r) \chi_1^{\pm 1/2}(\theta, \phi) \end{pmatrix} , \quad (23)$$

$$\psi_{\kappa=-1,W}^{\mu=\pm 1/2(e)}(r, \theta, \phi) = \begin{pmatrix} g_e^-(r) \chi_{-1}^{\pm 1/2}(\theta, \phi) \\ i f_e^-(r) \chi_1^{\pm 1/2}(\theta, \phi) \end{pmatrix} , \quad (24)$$

$$\psi_{\kappa=1,W}^{\mu=\pm 1/2(e)}(r, \theta, \phi) = \begin{pmatrix} g_e^+(r) \chi_1^{\pm 1/2}(\theta, \phi) \\ i f_e^+(r) \chi_{-1}^{\pm 1/2}(\theta, \phi) \end{pmatrix}. \quad (25)$$

In the above expression, we have neglected the electron mass, so that  $g_e^+$  and  $f_e^+$  are related to  $g_e^-$  and  $f_e^-$  as  $g_e^+ = i f_e^-$  and  $i f_e^+ = g_e^-$ . By integrating the Maxwell equations, the electric field  $E(r)$  is determined as

$$E(r) = \frac{Ze}{r^2} \int_0^r r'^2 \rho^{(p)}(r') dr'. \quad (26)$$

Once the proton and neutron densities are given, one can calculate the electric field  $E(r)$  by Eq.(26) and the electric potential  $V(r)$  by

$$V(r) = -e \int_r^\infty E(r') dr'. \quad (27)$$

The wave functions are then obtained by the Dirac equation Eq.(6), and the  $\mu$ - $e$  conversion rate is calculated by Eq.(14).

### 3 Numerical results

In order to evaluate Eq.(14), we need proton and neutron densities and the muon and electron wave functions. We first discuss proton and neutron densities and show the wave functions of muon and electron. Then, we present numerical results of the overlap integrals Eqs.(18) – (22) and the conversion rates for various nuclei.

#### 3.1 Distribution of protons and neutrons in nucleus

We have used proton density determined from electron scattering experiments. In the past, the charge density distribution of a nucleus was analyzed assuming some functional form of the proton distribution such as the two-parameter Fermi model, the three-parameter Fermi model, and the three-parameter Gaussian model. More recently, with improvement of experimental data, model-independent methods are used to extract detailed information on the density distribution. Examples are the Fourier-Bessel expansion and the sum of Gaussian functions. The proton density is very precisely determined when the model-independent analysis is carried out. We use the charge density listed in Ref.[20]. We adopt the results of the model-independent analyses when the data are available. More on charge distribution is described in Appendix A.

Determination of the neutron distribution is not as easy as that of the proton distribution [21]. There are several ways to determine the neutron density in the different region. Pionic atoms provide a probe of the neutron density on the periphery of the nucleus. In a certain level of the pionic atom the pion is absorbed by the nucleus. Since the strong interaction between the pion and the nucleus changes the energy and the width of this level, we can obtain information on the neutron density in the nucleus from the analysis of the atomic X-ray spectrum. Scattering experiments on the nucleus by strong interacting particles such as the proton and the alpha particle are also useful to determine the neutron density.

In this paper we use the following three methods to evaluate the  $\mu$ - $e$  conversion ratio because experimental data is not available for every nucleus:

1. First, we take the proton density from the electron scattering experiments given in Appendix A and assume the neutron density is the same as the proton density. For light nuclei this is a good approximation because the number of neutrons and protons are approximately equal and the conversion rates do not depend on the details of the neutron distribution. (method 1)
2. Second, we employ the nucleon distribution obtained from the pionic atom. We use the results of the analysis of Ref.[22], where the proton and neutron distributions are given in terms of the two-parameter Fermi function. (method 2)
3. Finally, we use the neutron distribution obtained from the polarized proton scattering experiment. The analysis was carried out for carbon (C) [23], titanium (Ti) [24], nickel (Ni) [23], zirconium (Zr) [23], and lead (Pb) [23] where proton and neutron density are given in the literature. We also estimate the uncertainty due to the error of the neutron distribution from the scattering experiment based on Refs.[25, 26]. (method 3)

The first method gives precise evaluation for the overlap integrals  $D$ ,  $S^{(p)}$  and  $V^{(p)}$ . On the other hand, neutron density is necessary in order to determine  $S^{(n)}$  and  $V^{(n)}$ . Although direct information on the neutron density is obtained from the proton scattering experiments, the data are available only for several nuclei. For comparison, we evaluate the conversion rates according to method 1 and method 2.

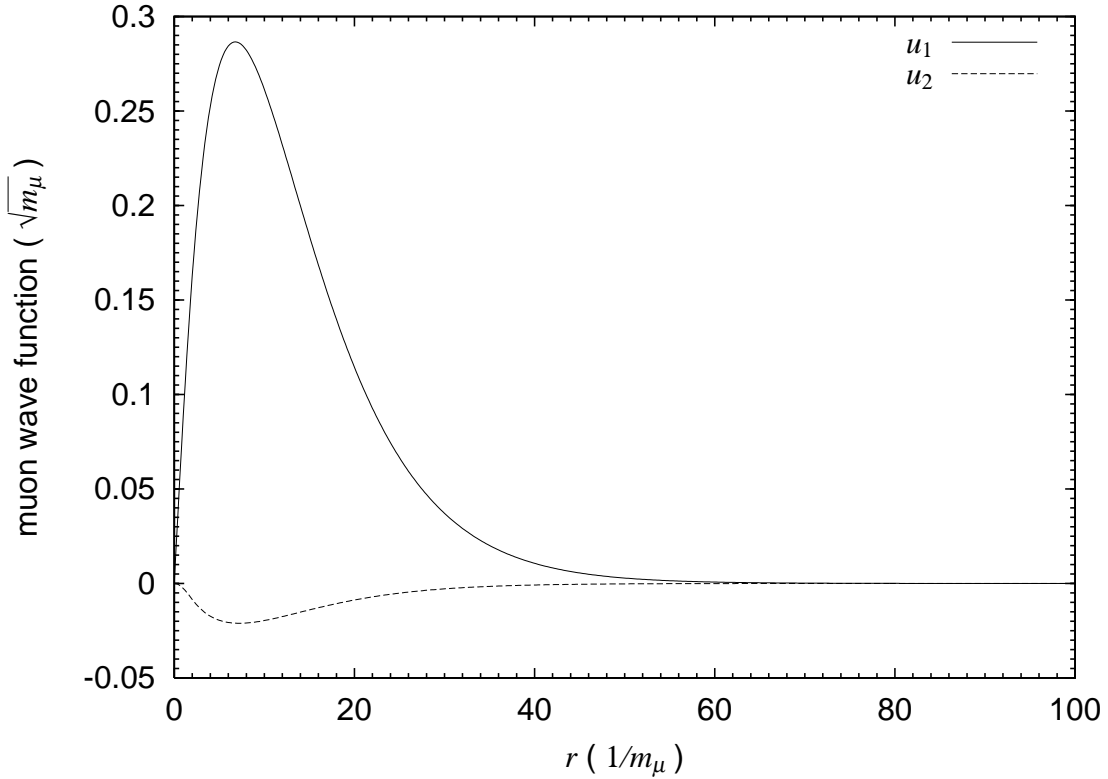


Figure 1: The normalized wave function of a muon in titanium (Ti) nucleus is plotted. The solid line and dashed line represent  $u_1(\equiv rg_\mu^-)$  and  $u_2(\equiv rf_\mu^-)$  components, respectively. The horizontal axis is the distance between the nucleus and the muon in the unit of  $1/m_\mu$ . The unit for the wave function is taken to be  $\sqrt{m_\mu}$ .

### 3.2 Numerical evaluation of the overlap integrals

In this subsection, we first show an example of the muon and electron wave functions obtained by solving the Dirac equation Eq.(2), and present the result of numerical calculation of overlap integrals  $D$ ,  $S^{(p,n)}$  and  $V^{(p,n)}$  defined by Eqs.(18) – (22).

The muon and electron wave functions are evaluated by solving the Dirac equation (2) with the electric potential given by Eq.(27). Ignoring the recoil of the nucleus which is of the order of  $m_\mu^2/M_N$ , where  $M_N$  is the nucleus mass, one finds that the energy of the out-going electron in Eq.(2) is equal to the muon mass minus the binding energy. As an example, we show the muon and electron wave functions in titanium (Ti) nucleus in Figs.1 and 2. We can see in Fig.1 that the lower component  $u_2$  in the muon wave function is much smaller than the upper component  $u_1$ . However, as pointed out in Ref.[14], its

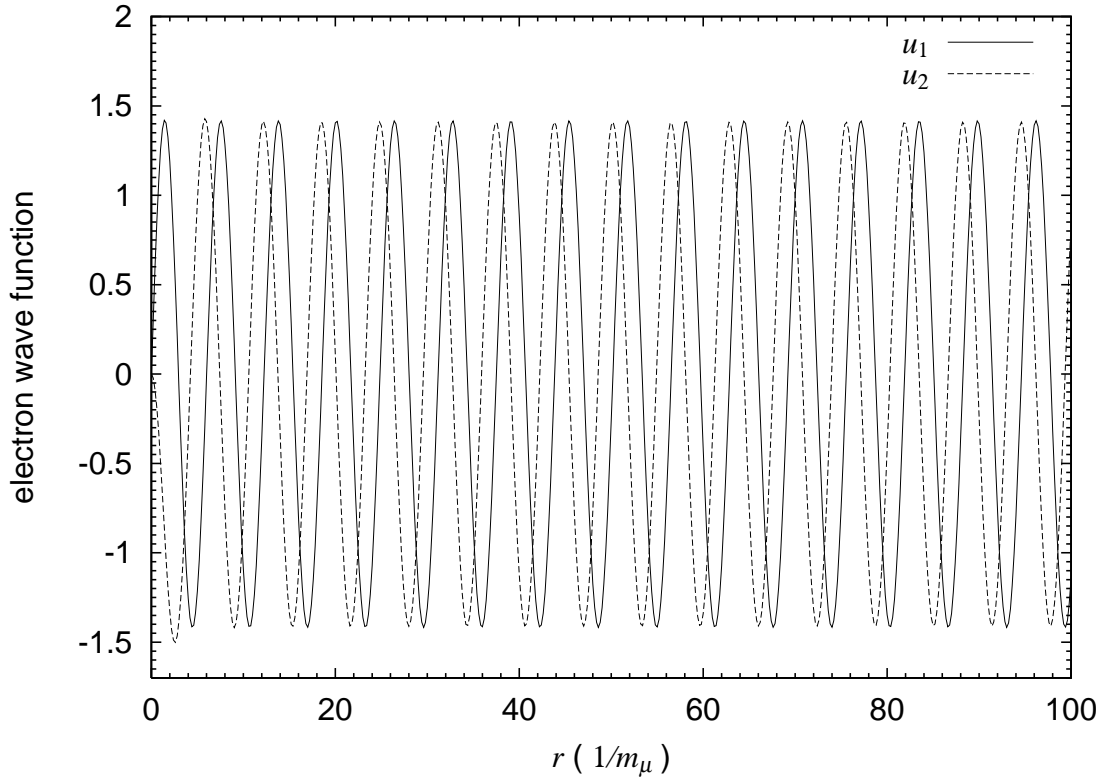


Figure 2: The normalized wave function of an electron in titanium (Ti) nucleus is plotted. The solid line and dashed line represent  $u_1(\equiv rg_e^-)$  and  $u_2(\equiv rf_e^-)$  components, respectively. The horizontal axis is the distance between the nucleus and the electron in the unit of  $1/m_\mu$ .

effect on the conversion rate is sizable for heavy nuclei. The overlap integrals are evaluated using these wave functions.

We present the numerical evaluation of the overlap integrals according to each of the three methods listed in the subsection 3.1. We present in Table 1 the results under the assumption  $\rho_n = \rho_p$ , where  $\rho_p$  is taken from Ref.[20] (method 1). We show in Fig.3 the  $Z$  dependences of the integrals. We omitted the points for  $^{166}_{68}\text{Er}$ ,  $^{181}_{73}\text{Ta}$ , and  $^{197}_{79}\text{Au}$  from this figure since these data are either obtained from quite old experiments or not well-established [20]. We see that the overlap integrals increases as functions of  $Z$  for light nuclei up to  $Z \sim 30$ , and saturate or decrease for heavy nuclei. This property can also be observed when we use the neutron density distribution based on method 2 and method 3 in subsection 3.1. We present in Table 2 and Fig.4 the results calculated using the analysis

Nucleus	$D$	$S^{(p)}$	$V^{(p)}$	$S^{(n)}$	$V^{(n)}$
$^4\text{He}$	0.0006	0.0003	0.0003	0.0003	0.0003
$^7\text{Li}$	0.0014	0.0006	0.0006	0.0008	0.0008
$^9\text{Be}$	0.0027	0.0011	0.0011	0.0014	0.0014
$^{11}\text{B}$	0.0047	0.0020	0.0020	0.0024	0.0024
$^{12}\text{C}$	0.0072	0.0031	0.0031	0.0031	0.0031
$^{14}\text{N}$	0.0103	0.0044	0.0044	0.0044	0.0044
$^{16}\text{O}$	0.0133	0.0057	0.0058	0.0057	0.0058
$^{19}\text{F}$	0.0166	0.0071	0.0072	0.0079	0.0081
$^{20}\text{Ne}$	0.0205	0.0088	0.0090	0.0088	0.0090
$^{24}\text{Mg}$	0.0312	0.0133	0.0138	0.0133	0.0138
$^{27}\text{Al}$	0.0362	0.0155	0.0161	0.0167	0.0173
$^{28}\text{Si}$	0.0419	0.0179	0.0187	0.0179	0.0187
$^{31}\text{P}$	0.0468	0.0201	0.0210	0.0214	0.0224
$^{32}\text{S}$	0.0524	0.0225	0.0236	0.0225	0.0236
$^{35}\text{Cl}$	0.0565	0.0241	0.0254	0.0256	0.0269
$^{40}\text{Ar}$	0.0621	0.0265	0.0281	0.0324	0.0343
$^{39}\text{K}$	0.0699	0.0299	0.0317	0.0314	0.0334
$^{40}\text{Ca}$	0.0761	0.0325	0.0347	0.0325	0.0347
$^{48}\text{Ti}$	0.0864	0.0368	0.0396	0.0435	0.0468
$^{51}\text{V}$	0.0931	0.0396	0.0428	0.0482	0.0521
$^{52}\text{Cr}$	0.100	0.0425	0.0461	0.0496	0.0538
$^{55}\text{Mn}$	0.107	0.0456	0.0496	0.0547	0.0596
$^{56}\text{Fe}$	0.110	0.0467	0.0512	0.0539	0.0591
$^{59}\text{Co}$	0.112	0.0471	0.0519	0.0558	0.0615
$^{58}\text{Ni}$	0.125	0.0527	0.0583	0.0565	0.0625
$^{63}\text{Cu}$	0.122	0.0514	0.0572	0.0603	0.0671
$^{64}\text{Zn}$	0.134	0.0561	0.0627	0.0636	0.0710
$^{74}\text{Ge}$	0.133	0.0554	0.0628	0.0727	0.0824
$^{80}\text{Se}$	0.146	0.0602	0.0690	0.0815	0.0933
$^{88}\text{Sr}$	0.163	0.0665	0.0778	0.0875	0.102
$^{89}\text{Y}$	0.164	0.0670	0.0788	0.0859	0.101

Table 1: The overlap integrals in the unit of  $m_\mu^{5/2}$  are listed. The proton distribution in the nuclei are taken from Ref.[20] (see also Appendix A), and neutron distribution are assumed to be same as that of protons (method 1 in subsection 3.1).

Nucleus	$D$	$S^{(p)}$	$V^{(p)}$	$S^{(n)}$	$V^{(n)}$
$^{90}_{40}\text{Zr}$	0.171	0.0697	0.0823	0.0872	0.103
$^{93}_{41}\text{Nb}$	0.171	0.0692	0.0823	0.0878	0.104
$^{98}_{42}\text{Mo}$	0.170	0.0683	0.0818	0.0911	0.109
$^{110}_{46}\text{Pd}$	0.176	0.0695	0.0855	0.0967	0.119
$^{114}_{48}\text{Cd}$	0.178	0.0696	0.0867	0.0958	0.119
$^{115}_{49}\text{In}$	0.181	0.0704	0.0882	0.0948	0.119
$^{120}_{50}\text{Sn}$	0.183	0.0707	0.0894	0.0990	0.125
$^{121}_{51}\text{Sb}$	0.195	0.0760	0.0957	0.104	0.131
$^{138}_{56}\text{Ba}$	0.184	0.0688	0.0911	0.101	0.133
$^{139}_{57}\text{La}$	0.189	0.0707	0.0937	0.102	0.135
$^{142}_{60}\text{Nd}$	0.183	0.0669	0.0909	0.0914	0.124
$^{152}_{62}\text{Sm}$	0.175	0.0631	0.0875	0.0915	0.127
$^{158}_{64}\text{Gd}$	0.173	0.0613	0.0865	0.0901	0.127
$^{165}_{67}\text{Ho}$	0.177	0.0617	0.0892	0.0902	0.131
$^{166}_{68}\text{Er}$	0.200	0.0693	0.101	0.0999	0.146
$^{181}_{73}\text{Ta}$	0.156	0.0513	0.0792	0.0759	0.117
$^{184}_{74}\text{W}$	0.156	0.0499	0.0794	0.0741	0.118
$^{197}_{79}\text{Au}$	0.189	0.0614	0.0974	0.0918	0.146
$^{204}_{80}\text{Hg}$	0.158	0.0482	0.0818	0.0746	0.127
$^{205}_{81}\text{Tl}$	0.161	0.0491	0.0834	0.0752	0.128
$^{208}_{82}\text{Pb}$	0.161	0.0488	0.0834	0.0749	0.128
$^{209}_{83}\text{Bi}$	0.159	0.0475	0.0826	0.0722	0.125
$^{232}_{90}\text{Th}$	0.154	0.0429	0.0809	0.0677	0.128
$^{238}_{92}\text{U}$	0.151	0.0417	0.0798	0.0662	0.127

Table 1: (Continued).

of the experiments of the pionic atom (method 2). As inputs of our calculation, we use the neutron matter parameter  $R_n$ [mean] in Table 4 of Ref.[22]. Table 3 and Fig.5 show the overlap integrals for the neutron density obtained from proton scattering experiments [23, 24] (method 3). The  $Z$  dependence shown in Figs.4 and 5 are similar to that seen in Fig.3.

As we can see in Fig.3, each overlap integral has different  $Z$  dependences. For example, the scalar ( $S^{(p,n)}$ ) and the vector ( $V^{(p,n)}$ ) type integrals are almost equal in light nuclei ( $Z \lesssim 30$ ), whereas the vector like integral is larger by a factor of 1.5 – 2 than the scalar one for heavy nuclei. This difference is due to the the relativistic effects of the muon wave functions which are significant in heavy nuclei. In fact, the scalar and vector overlap

Nucleus	$D$	$S^{(p)}$	$V^{(p)}$	$S^{(n)}$	$V^{(n)}$
$^{19}_9\text{F}$	0.0166	0.0071	0.0072	0.0089	0.0090
$^{23}_{11}\text{Na}$	0.0260	0.0111	0.0114	0.0128	0.0131
$^{24}_{12}\text{Mg}$	0.0299	0.0128	0.0132	0.0126	0.0131
$^{27}_{13}\text{Al}$	0.0357	0.0153	0.0159	0.0163	0.0169
$^{28}_{14}\text{Si}$	0.0421	0.0181	0.0188	0.0173	0.0180
$^{32}_{16}\text{S}$	0.0529	0.0227	0.0238	0.0221	0.0233
$^{40}_{18}\text{Ar}$	0.0628	0.0268	0.0284	0.0310	0.0330
$^{40}_{20}\text{Ca}$	0.0778	0.0333	0.0355	0.0319	0.0341
$^{56}_{26}\text{Fe}$	0.110	0.0464	0.0508	0.0503	0.0555
$^{63}_{29}\text{Cu}$	0.124	0.0521	0.0579	0.0585	0.0654
$^{74}_{32}\text{Ge}$	0.138	0.0576	0.0651	0.0704	0.0802
$^{75}_{33}\text{As}$	0.141	0.0585	0.0665	0.0690	0.0792
$^{142}_{58}\text{Ce}$	0.188	0.0698	0.0934	0.0844	0.117
$^{197}_{79}\text{Au}$	0.167	0.0523	0.0859	0.0610	0.108
$^{208}_{82}\text{Pb}$	0.162	0.0495	0.0838	0.0575	0.107
$^{209}_{83}\text{Bi}$	0.163	0.0495	0.0846	0.0579	0.108

Table 2: Same as Table 1, but here the results of the analysis of the pionic atom experiment are used for the distribution of the neutrons [22] (method 2 in subsection 3.1).

Nucleus	$D$	$S^{(p)}$	$V^{(p)}$	$S^{(n)}$	$V^{(n)}$
$^{12}_6\text{C}$	0.0074	0.0032	0.0032	0.0031	0.0032
$^{48}_{22}\text{Ti}$	0.0870	0.0371	0.0399	0.0462	0.0495
$^{58}_{28}\text{Ni}$	0.130	0.0548	0.0605	0.0606	0.0667
$^{90}_{40}\text{Zr}$	0.176	0.0715	0.0844	0.0841	0.100
$^{208}_{82}\text{Pb}$	0.156	0.0457	0.0812	0.0712	0.122

Table 3: Same as Table 1, but here the results of the analysis of the proton scattering experiments are used for the neutron density distribution [23, 24] (method 3 in subsection 3.1).

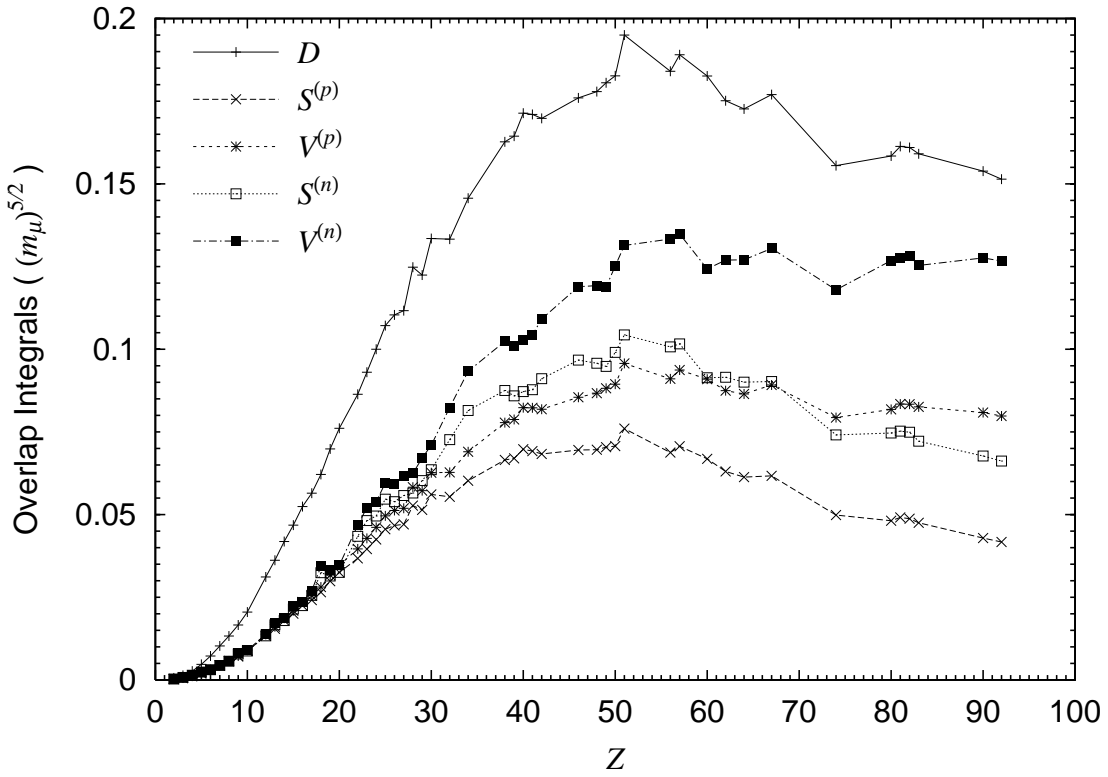


Figure 3: The overlap integrals are plotted as functions of the atomic number  $Z$ . Neutron density distributions are assumed to be equal to charge density distributions (method 1 in subsection 3.1).

integrals in Eqs.(19) and (21) [Eqs.(20) and (22)] are exactly the same, if we ignore the small component of the wave function  $f_\mu^-$ . For  $D$  we can show that  $D/(8e) \simeq S^{(p)} \simeq V^{(p)}$  are satisfied for light nuclei.

Comparing Tables 1, 2, and 3, one finds that the overlap integrals of the light nuclei agree with one another within a few percent. As for heavy nuclei,  $S^{(n)}$  and  $V^{(n)}$  have sizable difference. Taking  $^{208}\text{Pb}$  as an example, we find that the differences of  $S^{(n)}$  and  $V^{(n)}$  among the three methods turn out to be 30%, and 20%, respectively. The large difference of  $S^{(n)}$  and  $V^{(n)}$  implies that the overlap integrals are sensitive to the small variation of the neutron distribution for heavy nuclei. It is thus important to evaluate the ambiguity of the overlap integrals caused by the uncertainty of the distribution of the neutron.

In order to evaluate uncertainty from the neutron distribution determined by the

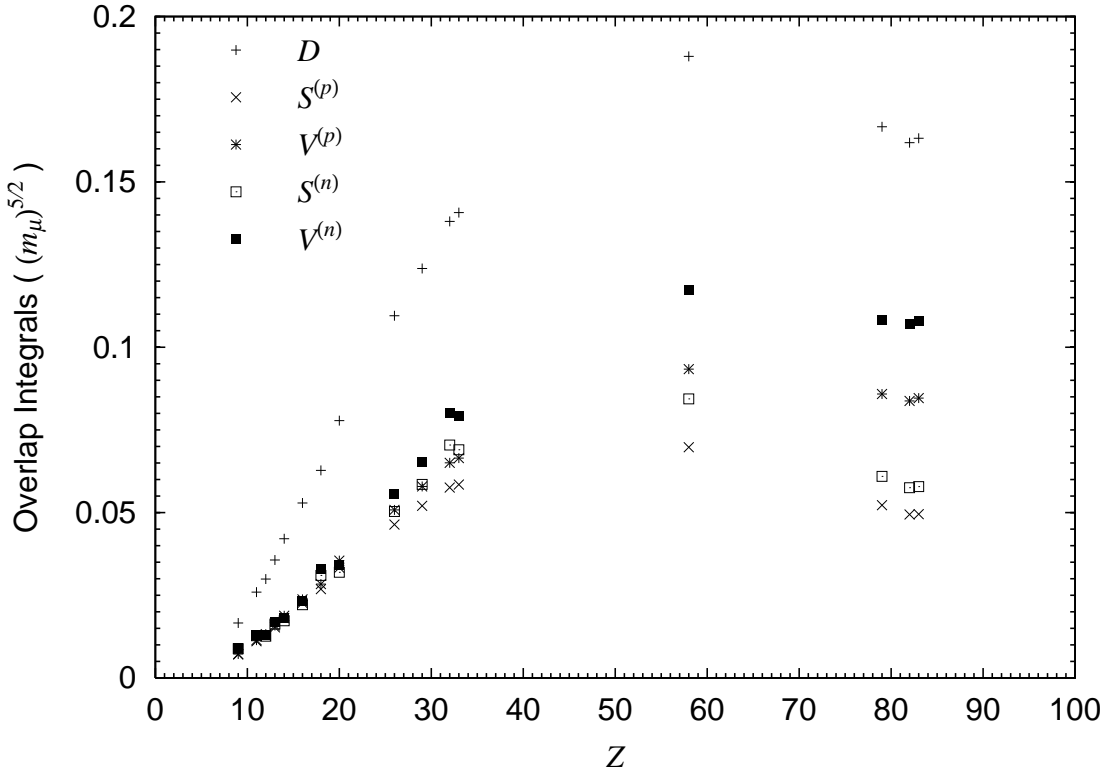


Figure 4: Same as Fig.3, but here the results of the analysis of the pionic atom experiment are used for the distribution of the neutrons [22] (method 2 in subsection 3.1).

proton experiments, we take several examples where the error of the neutron distribution is explicitly given in the literature. We calculated  $S^{(n)}$  and  $V^{(n)}$  within the uncertainty of the neutron distribution. For example, we present the error envelope of the neutron distribution in the nucleus  $^{208}_{82}\text{Pb}$  in Fig.6 [26]. The ambiguity of the neutron density distribution is large at the central region of the nucleus due to the poor statistics of the large angle scattering event. Similar envelopes are given in Ref.[25] for  $^{40}_{20}\text{Ca}$ ,  $^{58}_{28}\text{Ni}$ , and  $^{116}_{50}\text{Sn}$ . The overlap integrals evaluated using the minimum and maximum values of the envelope are shown in Table 4. In the evaluation of the overlap integrals we used the proton distribution listed in Table 5 since it is not explicitly given in the literature. The errors of  $S^{(n)}$  and  $V^{(n)}$  amount to a few percent for the light nuclei such as  $^{40}_{20}\text{Ca}$  and  $^{58}_{28}\text{Ni}$ , while they become 8.5% and 6.6% for  $^{116}_{50}\text{Sn}$  and 16.2% and 9.1% for  $^{208}_{82}\text{Pb}$ . This tendency is partly explained by the fact that the ambiguity of the neutron distribution is larger in the heavy nucleus. In addition, we see that the overlap between the wave functions and

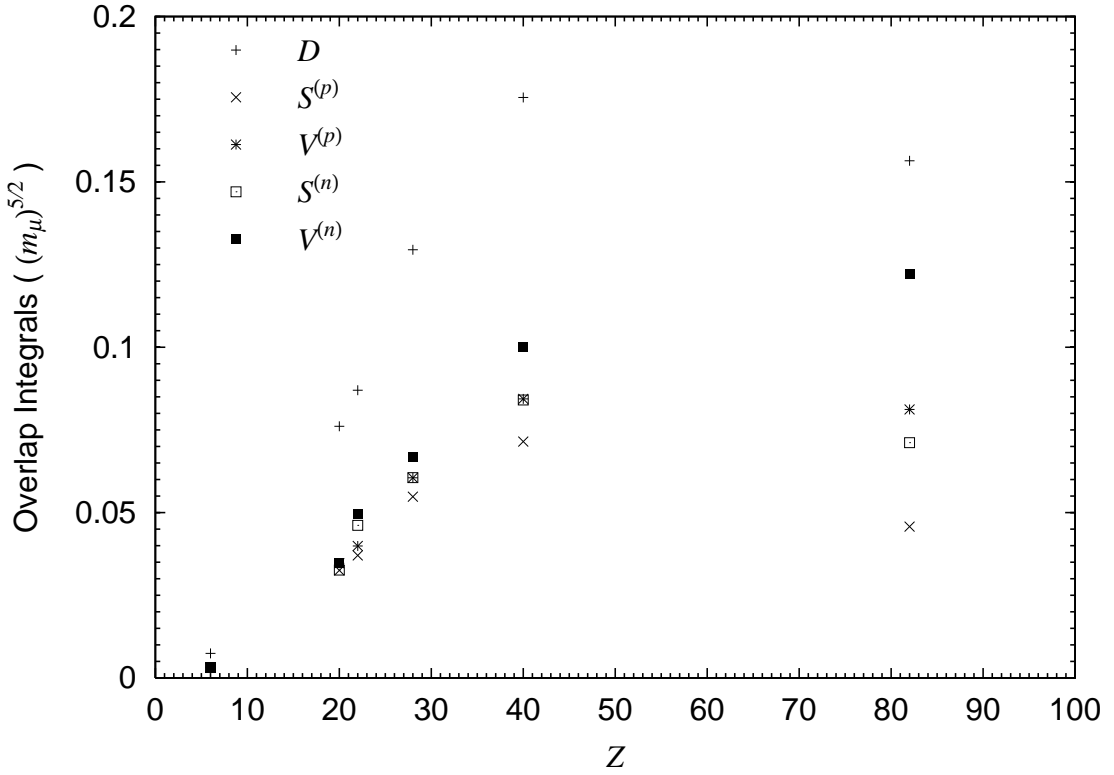


Figure 5: Same as Fig.3, but here the results of the analysis of the proton scattering experiments are used for the neutron density distribution [23, 24] (method 3 in subsection 3.1).

the nucleon density function become more sensitive to the neutron distribution for the heavy nucleus.

We can understand the  $Z$  dependences of the overlap integrals from the following consideration. When we adopt an approximation by Weinberg and Feinberg [12], where the muon wave function is replaced by the average value and the electron wave function is treated as a plane wave, the formula for the overlap integrals in Eqs.(19) and (21) are given by

$$V^{(p)} \sim S^{(p)} \sim \frac{1}{8\pi} \langle \phi_\mu \rangle Z F_p . \quad (28)$$

Here  $F_p$  is the form factor defined by

$$F_p = \int_0^\infty dr 4\pi r^2 \rho^{(p)}(r) \frac{\sin m_\mu r}{m_\mu r} , \quad (29)$$

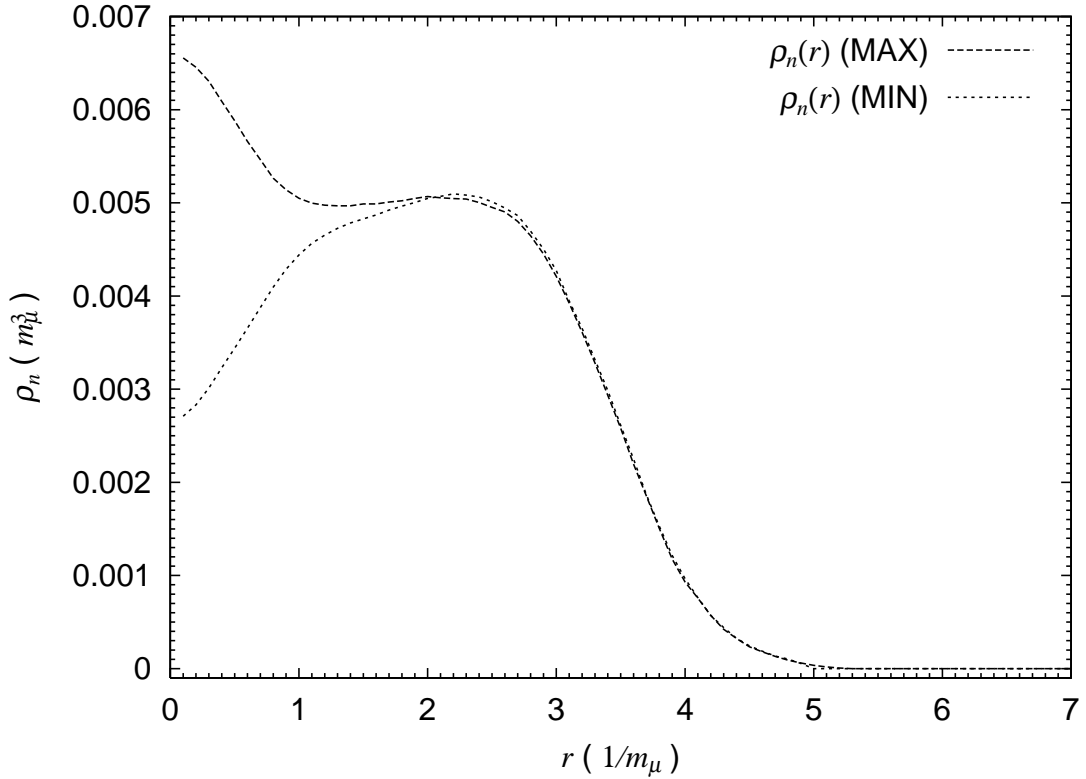


Figure 6: The error envelope of the neutron density distribution for  $^{208}_{82}\text{Pb}$  nucleus [26]. The poor statistics of the large angle scattering event leads to the large error at the central region.

and  $\langle \phi_\mu \rangle$  is the average value of the muon wave function in the nucleus given by

$$\langle \phi_\mu \rangle^2 = \int_0^\infty dr 4\pi r^2 (g_\mu^2 + f_\mu^2) \rho^{(p)} = \frac{4m_\mu^3 \alpha^3 Z_{\text{eff}}^4}{Z} . \quad (30)$$

In the last expression, we have introduced  $Z_{\text{eff}}$  which is the effective charge for the muon in the  $1s$  state. We show  $Z_{\text{eff}}$  in Fig.7. Since the muon wave function enter into the inside of the nucleus,  $Z_{\text{eff}}$  thus does not increase linearly with respect to  $Z$ . In Fig.8, we show the form factor  $F_p$  calculated based on method 1. There we see that  $F_p$  is a decreasing function and suppressed for heavy nuclei. These two properties explain the  $Z$  dependences of the overlap integrals.

		$S^{(n)}$	$V^{(n)}$	Ref.
$^{40}_{20}\text{Ca}$	Minimum	0.0331	0.0352	[25]
	Maximum	0.0338	0.0359	
$^{58}_{28}\text{Ni}$	Minimum	0.0584	0.0644	[25]
	Maximum	0.0592	0.0651	
$^{116}_{50}\text{Sn}$	Minimum	0.0958	0.120	[25]
	Maximum	0.104	0.128	
$^{208}_{82}\text{Pb}$	Minimum	0.0679	0.120	[26]
	Maximum	0.0789	0.131	

Table 4: Maximum and minimum values of the overlap integrals for the neutron density distribution, which is changed within the error envelope.

### 3.3 Numerical evaluation of conversion rate

It is now straightforward to evaluate the conversion rate through Eq.(14) once a theoretical model with LFV is specified. In this subsection, we present a  $\mu$ - $e$  conversion branching ratio for various types of LFV interactions in order to show the possibility to discriminate the different models through the  $Z$  dependence. We also compare our results with the existing calculations for the case where the photonic dipole operators are nonvanishing.

We consider the following three cases:

1. The photonic dipole operators  $A_L$  and/or  $A_R$  are nonvanishing. The  $\mu$ - $e$  conversion branching ratio is given by

$$B_{\mu N \rightarrow e N} \equiv \frac{\omega_{\text{conv}}}{\omega_{\text{capt}}} = \frac{2G_F^2 D^2 (|A_L|^2 + |A_R|^2)}{\omega_{\text{capt}}} , \quad (31)$$

where  $\omega_{\text{capt}}$  is the muon capture rate. For convenience, we list the capture rate in Appendix B [27].

2. The scalar operators  $g_{RS(d)}$  and/or  $g_{LS(d)}$  are nonvanishing. The  $\mu$ - $e$  conversion branching ratio in this case is given by

$$B_{\mu N \rightarrow e N} = \frac{2G_F^2 c_p^{(d)2} (S^{(p)} + S^{(n)})^2 (|g_{LS(d)}|^2 + |g_{RS(d)}|^2)}{\omega_{\text{capt}}} . \quad (32)$$

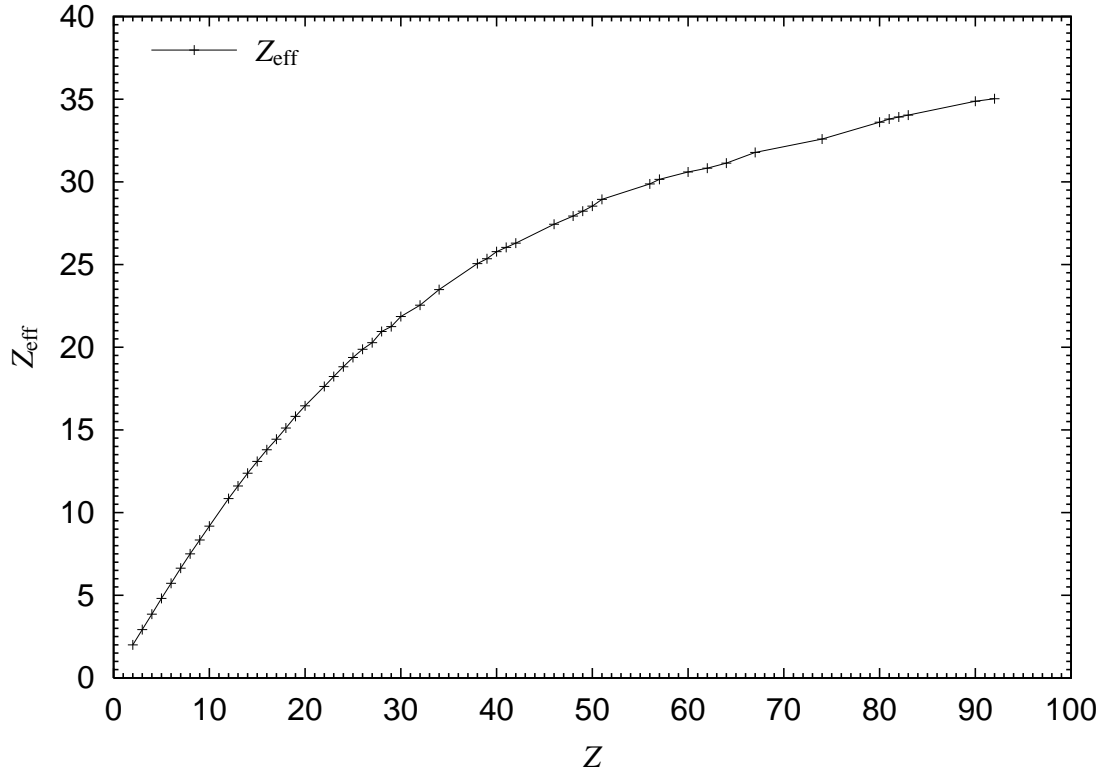


Figure 7: The effective charge for the muon in the  $1s$  state is plotted as a function of the atomic number  $Z$ .

3. The vector operators  $g_{RV(u)}$  and  $g_{LV(u)}$  satisfies  $g_{RV(u)} = -2g_{RV(d)} \neq 0$  and/or  $g_{LV(u)} = -2g_{LV(d)} \neq 0$ . The  $\mu$ - $e$  conversion branching ratio in this case is given by

$$B_{\mu N \rightarrow e N} = \frac{2G_F^2 V^{(p)2} (|\tilde{g}_{LV}^{(p)}|^2 + |\tilde{g}_{RV}^{(p)}|^2)}{\omega_{\text{capt}}}. \quad (33)$$

The first case appears as a good approximation in SUSY models for many cases, especially in SO(10) SUSY GUT models [4] and in SUSY models with right-handed neutrinos [6]. The second case is realized in some cases of SUSY models with R-parity violation [3]. The third case corresponds to the situation where the monopole form factors give dominant contributions in the  $\mu$ - $e$ - $\gamma$  transition. The  $\mu$ - $e$  conversion branching ratio are shown for three cases in Figs.9 (method 1), 10 (method 2), and 11 (method 3). In these figures the branching ratios are normalized by the value for aluminum evaluated by the method 1. We can see, for all three types, the branching ratio increases as  $Z$  for  $Z \lesssim 30$ , are largest for  $30 \lesssim Z \lesssim 60$ , and decreases for  $Z \gtrsim 60$ . It is also seen that the conversion

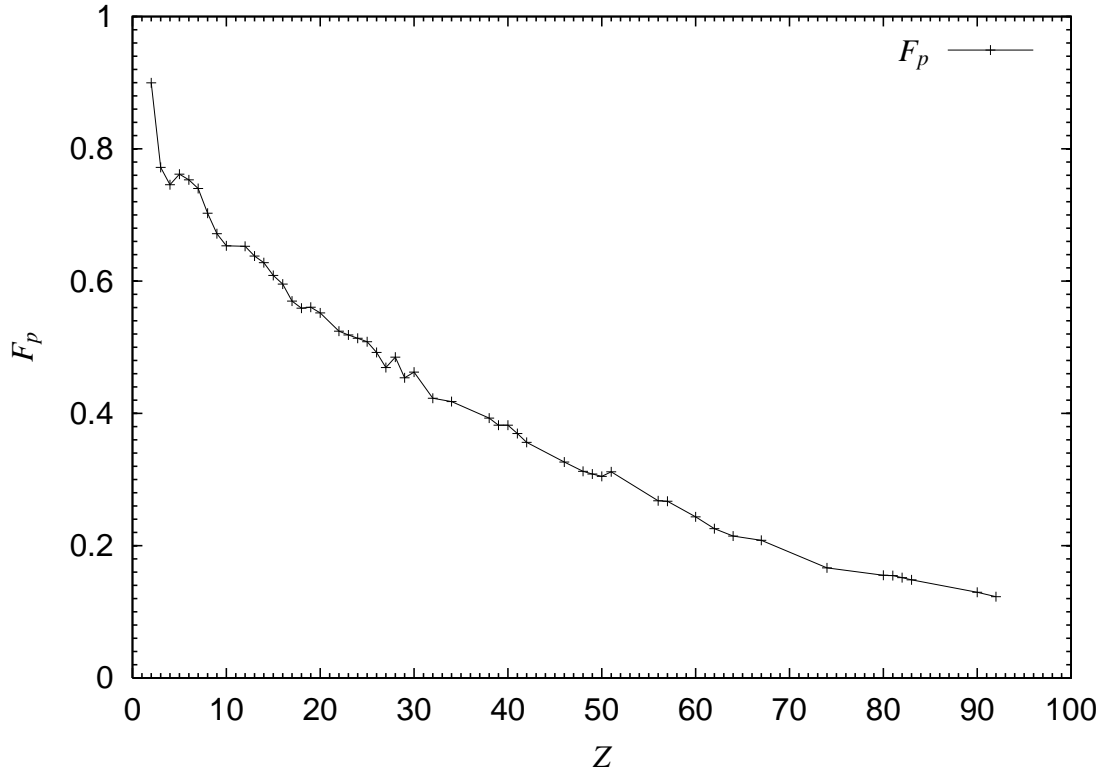


Figure 8: The form factor  $F_p$  is plotted as a function of the atomic number  $Z$ .

ratios have large differences in the heavy nuclei depending on three types of interactions. From this property we may be able to distinguish models beyond the SM through several experiments with different targets.

In order to see improvements of the present method from older calculations, we compare three different approximations for the case where the photonic dipole operators are nonvanishing: namely, our calculation, Weinberg-Feinberg approximation, and approximation by Shanker. For this purpose we define the ratio  $R(Z) \equiv B_{\mu N \rightarrow eN} / B(\mu \rightarrow e\gamma)$ , where the  $\mu \rightarrow e\gamma$  branching ratio  $B(\mu \rightarrow e\gamma)$  is given by  $384\pi^2(|A_L|^2 + |A_R|^2)$ . The present method thereby gives

$$R(Z) = \frac{G_F^2 D^2}{192\pi^2 \omega_{\text{capt}}} . \quad (34)$$

In the Weinberg-Feinberg calculation, the relativistic effects and the Coulomb distortion were ignored [12]. We define the conversion branching ratio  $B_{\mu N \rightarrow eN}^{\text{WF}}$  and the ratio of

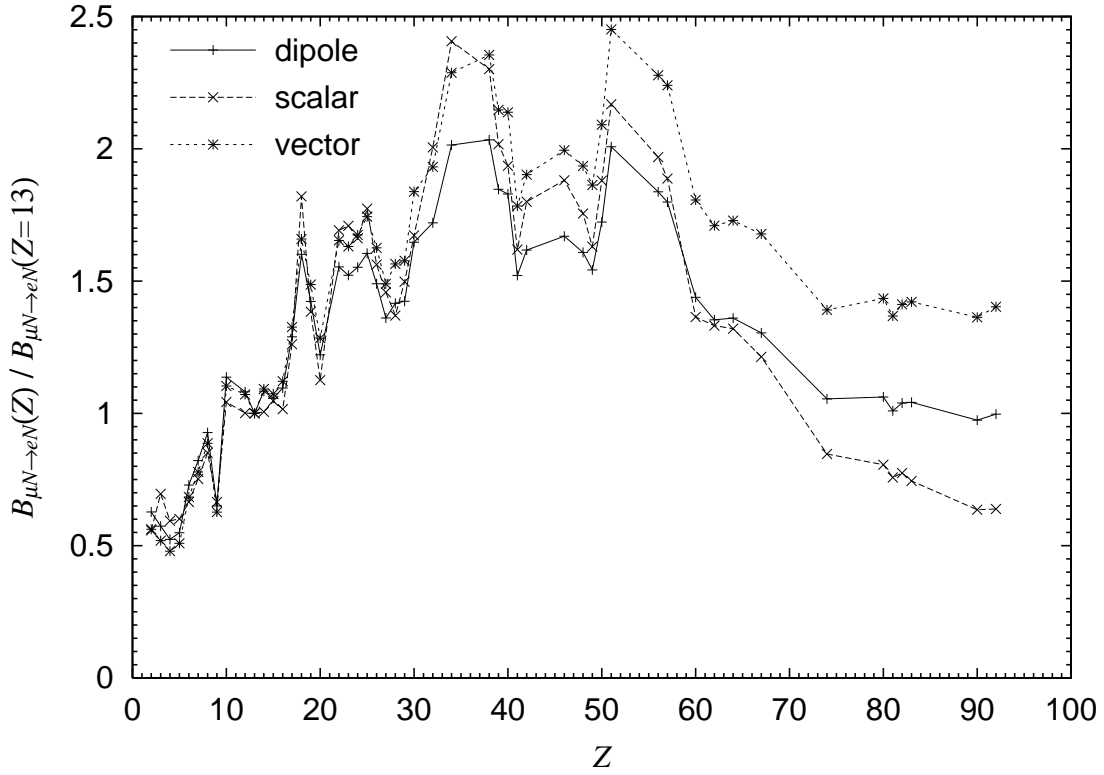


Figure 9: The  $\mu$ - $e$  conversion ratios for the typical theoretical models are plotted as functions of the atomic number  $Z$ . The solid, the long dashed, and the dashed lines represent the cases that the photonic dipole, scalar, and vector operator dominates, respectively. Proton and neutron distribution are taken according to method 1 in subsection 3.1, and the conversion ratios are normalized by the conversion ratio in aluminum nuclei ( $Z = 13$ ).

ratios  $R^{\text{WF}}(Z)$  in the Weinberg-Feinberg approximation by the following formula:

$$B_{\mu N \rightarrow eN}^{\text{WF}} = \frac{8G_F^2 m_\mu^5}{\pi^2} \alpha^3 Z_{\text{eff}}^4 Z F_p^2 (|A_L|^2 + |A_R|^2) \frac{1}{\omega_{\text{capt}}}, \quad (35)$$

$$R^{\text{WF}}(Z) = \frac{B_{\mu N \rightarrow eN}^{\text{WF}}}{B(\mu \rightarrow e\gamma)} = \frac{G_F^2 m_\mu^5 \alpha^3 Z_{\text{eff}}^4 Z F_p^2}{48\pi^4 \omega_{\text{capt}}}. \quad (36)$$

Notice that these are not exactly the same as the formula given in the original paper because they used approximate formula for the capture rate and the form factors for the general photonic transition. Shanker improved the Weinberg-Feinberg formula taking into account the relativistic effects and the Coulomb distortion. In his approximation, the branching ratio and the ratio of ratios for the dipole photonic interaction are given

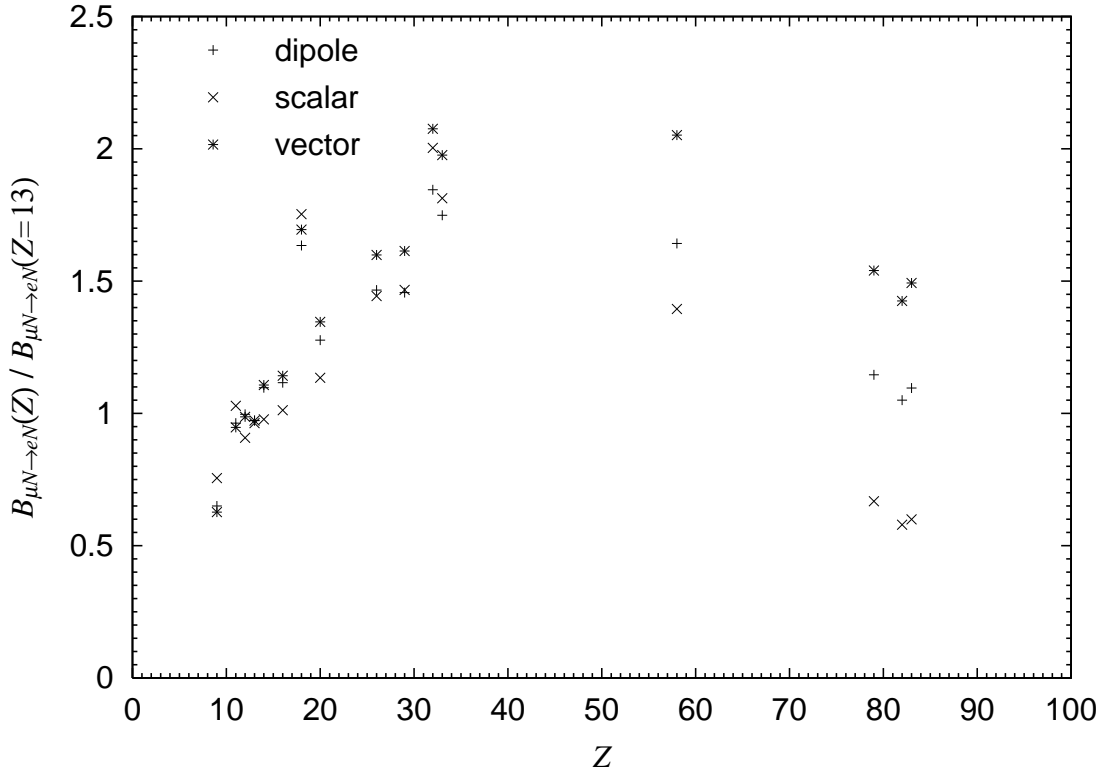


Figure 10: The  $\mu$ - $e$  conversion ratios for the typical theoretical models evaluated by the method 2 in subsection 3.1. The branching ratio is normalized by  $B_{\mu N \rightarrow eN}(Z = 13)$  evaluated by the method 1.

by

$$B_{\mu N \rightarrow eN}^S = 128e^2 G_F^2 V^{(p)2} (|A_L|^2 + |A_R|^2) \frac{1}{\omega_{\text{capt}}}, \quad (37)$$

$$R^S(Z) = \frac{B_{\mu N \rightarrow eN}^S}{B(\mu \rightarrow e\gamma)} = \frac{e^2 G_F^2 V^{(p)2}}{3\pi^2 \omega_{\text{capt}}} . \quad (38)$$

We present our  $R(Z)$ ,  $R^{\text{WF}}(Z)$ , and  $R^S(Z)$  in Fig.12. Here we used the proton density in the method 1 and the muon capture rate  $\omega_{\text{capt}}$  from the experiments [27]. We see that the three quantities have similar  $Z$  dependence: they range from 0.002 to 0.006, and are largest for  $Z = 30 - 60$ . The values of  $R^{\text{WF}}(Z)$  and  $R^S(Z)$  are larger than our  $R(Z)$  by 30% for  $Z \gtrsim 50$ . We have reproduced with a good accuracy the result by Czarnecki *et al.*, where they evaluated  $R(Z)$  for aluminum (Al), titanium (Ti), and lead (Pb) nuclei. Kosmas obtained in Ref.[17] the result that  $R(Z)$  is a monotonically increasing function, but he did not take into account the Coulomb distortion effect. We could indeed obtain

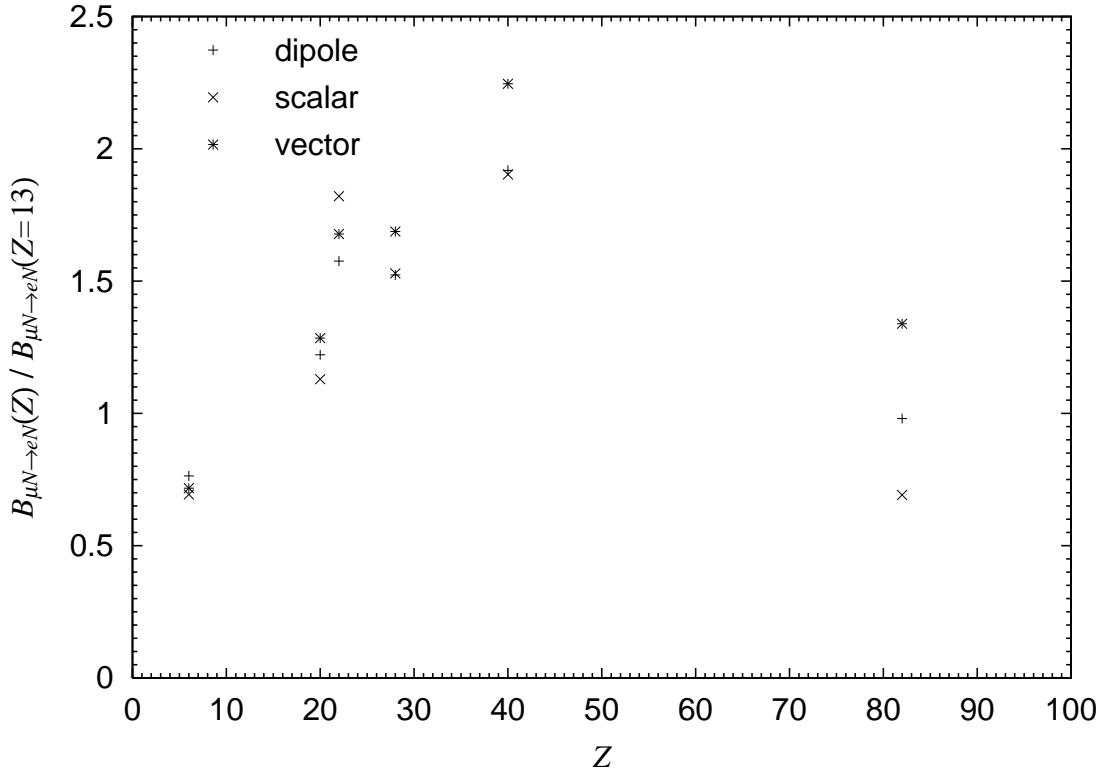


Figure 11: The  $\mu$ - $e$  conversion ratios for the typical theoretical models evaluated by the method 3 in subsection 3.1. The branching ratio is normalized by  $B_{\mu N \rightarrow e N}(Z = 13)$  evaluated by the method 1.

the increasing function of  $R(Z)$  by ignoring this effect. Thus the Coulomb distortion effect of the wave function is important in the calculation of the conversion rate for heavy nuclei, as noted by Shanker [14].

## 4 Summary

We have calculated the coherent  $\mu$ - $e$  conversion rate for general LFV interactions for various nuclei. We have used updated nuclear data for proton and neutron distributions and taken into account the ambiguity associated with neutron distribution. We gave the list of the overlap integrals in Tables 1, 2, and 3 for various nuclei, from which we can calculate conversion rates for general interaction for LFV using Eq.(14). We also investigate  $Z$  dependence of the conversion rate. We see that the branching ratio increases

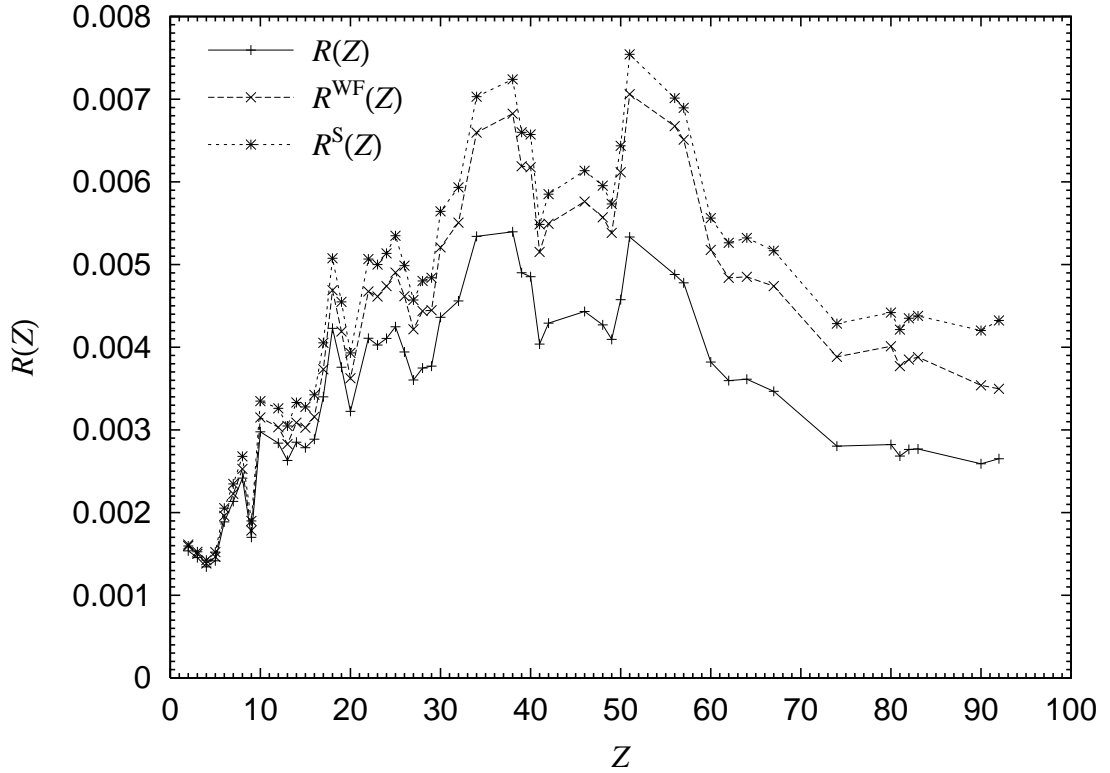


Figure 12: The  $\mu$ - $e$  conversion branching ratio divided by the  $\mu \rightarrow e\gamma$  decay branching ratio for method 1 is plotted as a function of atomic number  $Z$ . The solid line ( $R(Z)$ ), the long-dashed line ( $R^{\text{WF}}(Z)$ ), and the dashed line ( $R^S(Z)$ ) represent the results of our calculation, the Weinberg-Feinberg formula, and the Shanker's approximation, respectively.

for the light nuclei such as  $Z \lesssim 30$ , are largest for  $Z = 30 - 60$ , and decreases for heavy nuclei with  $Z \gtrsim 60$ . Although this tendency of  $Z$  dependence is the same for different types of coupling constants, there are significant difference in  $Z$  dependence of branching ratios. We show that the ambiguity in the calculation of the overlapping integrals associated with proton densities ( $D$ ,  $S^{(p)}$ , and  $V^{(p)}$ ) is quite small because the charge density of nuclei are well known. On the other hand, the overlapping integrals  $S^{(n)}$  and  $V^{(n)}$  contain sizable uncertainty of 10% – 15% for heavy nuclei from neutron distribution, whereas the corresponding uncertainty is a few percent for light nuclei. Because the main ambiguity for heavy nuclei is associated with neutron density, it will be possible to make a more precise prediction if we can determine the neutron density with improved analyses and experiments.

The results of our calculation are useful to choose the appropriate target nuclei for future experiments for the  $\mu$ - $e$  conversion search. In addition, it may be possible to identify the theoretical models beyond the Standard Model through the  $Z$  dependence of different interactions when the signal of the  $\mu$ - $e$  conversion is experimentally observed.

## Acknowledgments

We would like to thank J. Hisano for useful discussions. This work was supported by the JSPS Research Fellowships for Young Scientists (R. K. and M. K.). The work of Y. O. was supported in part by a Grant-in-Aid of the Ministry of Education, Culture, Sports, Science and Technology, Government of Japan (No. 13640309), priority area “Supersymmetry and Unified Theory of Elementary Particles” (No. 707).

## A Proton and neutron densities in nuclei

We introduce models of nucleon densities in nuclei and list the values of parameters of these models used in the calculation.

We used one of the following models for each nucleus [20].

1. Harmonic oscillator model (HO):

$$\rho_{p(n)}(r) = \rho_0 \left[ 1 + \alpha \left( \frac{r}{a} \right)^2 \right] \exp \left[ - \left( \frac{r}{a} \right)^2 \right]. \quad (39)$$

2. Two-parameter Fermi model (2pF):

$$\rho_{p(n)}(r) = \frac{\rho_0}{1 + \exp[(r - c_{p(n)})/z_{p(n)}]} . \quad (40)$$

3. Three-parameter Fermi model (3pF):

$$\frac{\rho_0 (1 + w_{p(n)} r^2 / c_{p(n)}^2)}{1 + \exp[(r - c_{p(n)})/z_{p(n)}]} . \quad (41)$$

4. Two-parameter Gaussian model (2pG):

$$\rho_{p(n)}(r) = \frac{\rho_0}{1 + \exp[(r^2 - c_{p(n)}^2)/z_{p(n)}^2]} . \quad (42)$$

5. Three-parameter Gaussian model (3pG):

$$\rho_{p(n)}(r) = \frac{\rho_0(1 + w_{p(n)}r^2/c_{p(n)}^2)}{1 + \exp[(r^2 - c_{p(n)}^2)/z_{p(n)}^2]} . \quad (43)$$

Here  $c_{p(n)}$ ,  $z_{p(n)}$ , and  $w_{p(n)}$  are the model parameters and  $\rho_0$  is the normalization constant. We also used the following model-independent analysis for several nuclei.

6. The Fourier-Bessel expansion (FB):

$$\rho_{p(n)}(r) = \begin{cases} \sum_v a_v j_0(v\pi r/R) & \text{for } r \leq R \\ 0 & \text{for } r > R \end{cases} , \quad (44)$$

where  $a_v$  are the coefficients,  $R$  is the cutoff radius, and the function  $j_0(z) = \sin z/z$  is the spherical Bessel function of the zeroth order.

7. The Sum of Gaussian expansion (SOG):

$$\rho_{p(n)}(r) = \sum_i A_i \left\{ \exp \left[ - \left( \frac{r - R_i}{\gamma} \right)^2 \right] + \exp \left[ - \left( \frac{r + R_i}{\gamma} \right)^2 \right] \right\} , \quad (45)$$

where

$$A_i = \frac{ZeQ_i}{2\pi^{3/2}\gamma^3(1 + 2R_i^2/\gamma^2)} . \quad (46)$$

We list the model and its parameters used in calculation in Table 5. We do not list parameters for FB and SOG there; see Ref.[20].

## B Muon capture rate in nuclei

We list in Table 6 the muon capture rates  $\omega_{\text{capt}}$  which are used in our calculation [27].

## References

- [1] For review, see Y. Kuno and Y. Okada, Rev. Mod. Phys. **73**, 151 (2001).
- [2] A. E. Faraggi and M. Pospelov, Phys. Lett. B **458**, 237 (1999);  
R. Kitano, Phys. Lett. B **481**, 39 (2000).
- [3] J. E. Kim, P. Ko and D. G. Lee, Phys. Rev. D **56**, 100 (1997);  
K. Huitu, J. Maalampi, M. Raidal and A. Santamaria, Phys. Lett. B **430**, 355 (1998);  
A. Faessler, T. S. Kosmas, S. Kovalenko and J. D. Vergados, Nucl. Phys. B **587**, 25 (2000);  
A. de Gouvea, S. Lola and K. Tobe, Phys. Rev. D **63**, 035004 (2001).
- [4] R. Barbieri, L. J. Hall and A. Strumia, Nucl. Phys. B **445**, 219 (1995).
- [5] R. Barbieri and L. J. Hall, Phys. Lett. B **338**, 212 (1994);  
J. Hisano, T. Moroi, K. Tobe and M. Yamaguchi, Phys. Lett. B **391**, 341 (1997)  
[Erratum-ibid. B **397**, 357 (1997)];  
Y. Okada, K. i. Okumura and Y. Shimizu, Phys. Rev. D **58**, 051901 (1998);  
Y. Okada, K. i. Okumura and Y. Shimizu, Phys. Rev. D **61**, 094001 (2000).
- [6] F. Borzumati and A. Masiero, Phys. Rev. Lett. **57**, 961 (1986);  
J. Hisano, T. Moroi, K. Tobe, M. Yamaguchi and T. Yanagida, Phys. Lett. **B357**, 579 (1995);  
J. Hisano, T. Moroi, K. Tobe and M. Yamaguchi, Phys. Rev. **D53**, 2442 (1996);  
J. Hisano, D. Nomura and T. Yanagida, Phys. Lett. **B437**, 351 (1998);  
J. Hisano, D. Nomura, Y. Okada, Y. Shimizu and M. Tanaka, Phys. Rev. D **58**, 116010 (1998);  
J. Hisano and D. Nomura, Phys. Rev. **D59**, 116005 (1999);  
W. Buchmuller, D. Delepine and F. Vissani, Phys. Lett. **B459**, 171 (1999);  
J. Ellis, M. E. Gomez, G. K. Leontaris, S. Lola and D. V. Nanopoulos, Eur. Phys. J. **C14**, 319 (2000);  
W. Buchmuller, D. Delepine and L. T. Handoko, Nucl. Phys. **B576**, 445 (2000);  
J. Sato, K. Tobe and T. Yanagida, Phys. Lett. B **498**, 189 (2001);

J. Sato and K. Tobe, Phys. Rev. D **63**, 116010 (2001);  
 A. Kageyama, S. Kaneko, N. Shimoyama and M. Tanimoto, Phys. Lett. B **527**, 206 (2002);  
 J. R. Ellis, J. Hisano, S. Lola and M. Raidal, Nucl. Phys. B **621**, 208 (2002).

[7] M. L. Brooks *et al.* [MEGA Collaboration], Phys. Rev. Lett. **83**, 1521 (1999).

[8] L. M. Barkov *et al.*, research proposal to PSI;  
 S. Ritt, in Proceedings of *The 2nd International Workshop on Neutrino Oscillations and their Origin*, edited by Y. Suzuki *et al.* (World Scientific), p. 245 (2000).

[9] P. Wintz, in Proceedings of *the First International Symposium on Lepton and Baryon Number Violation*, edited by H. V. Klapdor-Kleingrothaus and I. V. Krivosheina (Institute of Physics, Bristol/Philadelphia), p. 534 (1998).

[10] M. Bachman *et al.* [MECO Collaboration], experimental proposal E940 to Brookhaven National Laboratory AGS (1997).

[11] Y. Kuno, in Proceedings of *The 2nd International Workshop on Neutrino Oscillations and their Origin*, edited by Y. Suzuki *et al.* (World Scientific), p. 253 (2000).

[12] S. Weinberg and G. Feinberg, Phys. Rev. Lett. **3** 111 (1959).

[13] W. J. Marciano and A. I. Sanda, Phys. Rev. Lett. **38**, 1512 (1977).

[14] O. Shanker, Phys. Rev. D **20**, 1608 (1979).

[15] A. Czarnecki, W. J. Marciano and K. Melnikov, arXiv:hep-ph/9801218;  
 A. Czarnecki, W. J. Marciano and K. Melnikov, in *Proceedings of Workshop on Physics at the First Muon Collider and at the Front End of the Muon Collider*, Fermilab, edited by S. H. Geer and R. Raja, AIP Conf. Proc. No. 435 (AIP, New York), p. 409.

[16] H. C. Chiang, E. Oset, T. S. Kosmas, A. Faessler and J. D. Vergados, Nucl. Phys. A **559**, 526 (1993);  
 T. S. Kosmas, J. D. Vergados, O. Civitarese, and A. Faessler, Nucl. Phys. A **570**,

637 (1994);

T. S. Kosmas and J. D. Vergados, Phys. Rept. **264**, 251 (1996);

T. S. Kosmas, J. D. Vergados and A. Faessler, Phys. Atom. Nucl. **61**, 1161 (1998);

T. Kosmas, Z. Ren and A. Faessler, Nucl. Phys. A **665**, 183 (2000). T. Siiskonen, J. Suhonen and T. S. Kosmas, Phys. Rev. C **62**, 035502 (2000).

[17] T. S. Kosmas, arXiv:nucl-th/0108045.

[18] M. E. Rose, *Relativistic Electron Theory* (John Wiley, New York, 1961).

[19] T. S. Kosmas, S. Kovalenko and I. Schmidt, Phys. Lett. B **511**, 203 (2001).

[20] C. W. De Jager, H. De Vries and C. De Vries, Atom. Data Nucl. Data Tabl. **36** (1987) 495;

G. Fricke *et al.*, Atom. Data Nucl. Data Tabl. **60**, 177 (1995).

[21] C. J. Batty, E. Friedman, H. J. Gils and H. Rebel, in *Advances in Nuclear Physics*, Vol. 19, edited by J. W. Negele and E. Vogt (Plenum Press, New York), p. 1 (1989).

[22] C. Garcia-Recio, J. Nieves, and E. Oset, Nucl. Phys. **A547**, 473 (1992).

[23] L. Ray, G. W. Hoffmann, G. S. Blanpied, W. R. Coker and R. P. Liljestrand, Phys. Rev. C **18**, 1756 (1978).

[24] G. Pauletta *et al.*, Phys. Lett. B **106**, 470 (1981).

[25] L. Ray, Phys. Rev. C **19**, 1855 (1979).

[26] G. W. Hoffmann *et al.*, Phys. Rev. C **21**, 1488 (1980).

[27] T. Suzuki, D. F. Measday and J. P. Roalsvig, Phys. Rev. C **35**, 2212 (1987).

Nucleus	Model	$c_p$ or $a_p$ (fm)	$z_p$ (fm) or $\alpha$	$w_p$
$^4_2\text{He}$	SOG	—	—	—
$^7_3\text{Li}$	HO	1.77	0.327	—
$^9_4\text{Be}$	HO	1.791	0.611	—
$^{11}_5\text{B}$	HO	1.69	0.811	—
$^{12}_6\text{C}$	FB	—	—	—
$^{14}_7\text{N}$	3pF	2.570	0.5052	-0.180
$^{16}_8\text{O}$	FB	—	—	—
$^{19}_9\text{F}$	2pF	2.59	0.564	—
$^{20}_{10}\text{Ne}$	3pF	2.791	0.698	-0.168
$^{24}_{12}\text{Mg}$	3pF	2.791	0.698	-0.168
$^{27}_{13}\text{Al}$	FB	—	—	—
$^{28}_{14}\text{Si}$	3pF	3.340	0.580	-0.233
$^{31}_{15}\text{P}$	FB	—	—	—
$^{32}_{16}\text{S}$	FB	—	—	—
$^{35}_{17}\text{Cl}$	3pF	3.476	0.599	-0.10
$^{40}_{18}\text{Ar}$	FB	—	—	—
$^{39}_{19}\text{K}$	3pF	3.743	0.585	-0.201
$^{40}_{20}\text{Ca}$	FB	—	—	—
$^{48}_{22}\text{Ti}$	FB	—	—	—
$^{51}_{23}\text{V}$	2pF	3.91	0.532	—
$^{52}_{24}\text{Cr}$	FB	—	—	—
$^{55}_{25}\text{Mn}$	2pF	3.89	0.567	—
$^{56}_{26}\text{Fe}$	3pG	3.505	2.325	0.380
$^{59}_{27}\text{Co}$	2pF	4.158	0.575	—
$^{58}_{28}\text{Ni}$	FB	—	—	—
$^{63}_{29}\text{Cu}$	2pF	4.218	0.596	—
$^{64}_{30}\text{Zn}$	3pG	3.664	2.425	0.342
$^{74}_{32}\text{Ge}$	FB	—	—	—
$^{80}_{34}\text{Se}$	2pG	4.622	2.365	—
$^{88}_{38}\text{Sr}$	FB	—	—	—
$^{89}_{39}\text{Y}$	2pF	4.86	0.542	—
$^{90}_{40}\text{Zr}$	FB	—	—	—

Table 5: The model parameters of the proton density functions are listed. These values are extracted from Refs.[20]. The abbreviations HO, 2pF, 3pF, 2pG, 3pG, FB, and SOG represent the harmonic oscillator model, the two-parameter Fermi model, the three-parameter Fermi model, the two-parameter Gaussian model, the three-parameter Gaussian model, the Fourier-Bessel expansion, and sum of Gaussian, respectively. We do not list here parameters for FB and SOG; see Ref.[20].

Nucleus	Model	$c_p$ or $a_p$ (fm)	$z_p$ or $\alpha$ (fm)	$w_p$
$^{93}\text{Nb}$	2pF	4.953	0.541	—
$^{41}\text{K}$	FB	—	—	—
$^{98}\text{Mo}$	FB	—	—	—
$^{42}\text{Ca}$	FB	—	—	—
$^{110}\text{Pd}$	FB	—	—	—
$^{46}\text{Cr}$	2pF	5.314	0.571	—
$^{48}\text{Cd}$	2pF	5.357	0.563	—
$^{115}\text{In}$	2pF	5.110	2.619	0.292
$^{49}\text{As}$	3pG	5.32	0.57	—
$^{120}\text{Sn}$	3pG	5.3376	2.6776	0.3749
$^{50}\text{Ni}$	2pF	5.71	0.535	—
$^{121}\text{Sb}$	2pF	5.839	0.569	—
$^{56}\text{Ba}$	FB	—	—	—
$^{139}\text{La}$	FB	—	—	—
$^{142}\text{Nd}$	FB	—	—	—
$^{60}\text{Ni}$	2pF	6.12	0.57	—
$^{152}\text{Sm}$	3pF	5.98	0.446	0.19
$^{62}\text{Ni}$	2pF	6.38	0.64	—
$^{64}\text{Gd}$	2pF	6.51	0.535	—
$^{165}\text{Ho}$	2pF	6.38	0.535	—
$^{67}\text{Cu}$	FB	—	—	—
$^{166}\text{Er}$	FB	—	—	—
$^{181}\text{Ta}$	FB	—	—	—
$^{184}\text{W}$	FB	—	—	—
$^{74}\text{Cr}$	2pF	6.851	0.518	—
$^{197}\text{Au}$	2pF	6.874	0.556	—
$^{204}\text{Hg}$	FB	—	—	—
$^{205}\text{Tl}$	SOG	—	—	—
$^{81}\text{Y}$	FB	—	—	—
$^{208}\text{Pb}$	FB	—	—	—
$^{82}\text{Se}$	FB	—	—	—
$^{209}\text{Bi}$	FB	—	—	—
$^{83}\text{Rb}$	2pF	—	—	—
$^{232}\text{Th}$	2pF	—	—	—
$^{90}\text{Zr}$	2pF	—	—	—
$^{238}\text{U}$	2pF	—	—	—

Table 5: (Continued).

Nucleus	$\omega_{\text{capt}} (10^6 \text{s}^{-1})$	Nucleus	$\omega_{\text{capt}} (10^6 \text{s}^{-1})$
$^{12}\text{C}$	0.0388	$^{88}\text{Sr}$	7.02
$^{14}\text{N}$	0.0693	$^{89}\text{Y}$	7.89
$^{16}\text{O}$	0.1026	$^{90}\text{Zr}$	8.66
$^{19}\text{F}$	0.229	$^{93}\text{Nb}$	10.36
$^{20}\text{Ne}$	0.200	$^{92}\text{Mo}$	9.614
$^{23}\text{Na}$	0.3772	$^{110}\text{Pd}$	10.00
$^{24}\text{Mg}$	0.4841	$^{114}\text{Cd}$	10.61
$^{27}\text{Al}$	0.7054	$^{115}\text{In}$	11.40
$^{28}\text{Si}$	0.8712	$^{120}\text{Sn}$	10.44
$^{31}\text{P}$	1.1185	$^{121}\text{Sb}$	10.21
$^{32}\text{S}$	1.352	$^{138}\text{Ba}$	9.94
$^{35}\text{Cl}$	1.333	$^{139}\text{La}$	10.71
$^{40}\text{Ar}$	1.30	$^{140}\text{Ce}$	11.60
$^{39}\text{K}$	1.849	$^{142}\text{Nd}$	12.50
$^{40}\text{Ca}$	2.557	$^{152}\text{Sm}$	12.22
$^{48}\text{Ti}$	2.59	$^{158}\text{Gd}$	11.82
$^{51}\text{V}$	3.069	$^{165}\text{Ho}$	12.95
$^{52}\text{Cr}$	3.472	$^{166}\text{Er}$	13.04
$^{55}\text{Mn}$	3.857	$^{181}\text{Ta}$	12.86
$^{56}\text{Fe}$	4.411	$^{184}\text{W}$	12.36
$^{59}\text{Co}$	4.940	$^{197}\text{Au}$	13.07
$^{58}\text{Ni}$	5.932	$^{205}\text{Tl}$	13.90
$^{63}\text{Cu}$	5.676	$^{207}\text{Pb}$	13.45
$^{64}\text{Zn}$	5.834	$^{209}\text{Bi}$	13.10
$^{72}\text{Ge}$	5.569	$^{232}\text{Th}$	13.1
$^{75}\text{As}$	6.104	$^{238}\text{U}$	12.4

Table 6: The total capture rates used in calculation are listed [27].